Article

Influence of Heat Treatment and High-Pressure Torsion on Phase Transformations in TiZrHfMoCr High-Entropy Alloy

Alena Gornakova [1], Boris Straumal [1,2,*], Alexei Kuzmin [3], Alexander Tyurin [4], Elena Chernyaeva [5], Alexander Druzhinin [1], Natalia Afonikova [1] and Gregory Davdian [1,2]

[1] Ospina Institute of Solid State Physics of the Russian Academy of Sciences, Ac. Osipyan Str. 2, 142432 Chernogolovka, Russia; alenahas@issp.ac.ru (A.G.); druzhinin@issp.ac.ru (A.D.); natasha@issp.ac.ru (N.A.); faberest@yandex.ru (G.D.)

[2] Department of Physical Chemistry, National University of Science and Technology "MISIS", Leninsky Avenue 4, 119991 Moscow, Russia

[3] Institute of Solid State Physics, University of Latvia, Kengaraga Str. 8, LV-1063 Riga, Latvia; a.kuzmin@cfi.lu.lv

[4] G.R. Derzhavin Research Institute "Nanotechnologies and Nanomaterials" TSU, Internazionalnaja Str. 30, 392000 Tambov, Russia; tyurin@tsu.tmb.ru

[5] Department of Elasticity Therory, St. Petersburg University, 7-9 Universitetskaya Embarkment, 199034 St. Petersburg, Russia; lena@smel.math.spbu.ru

* Correspondence: straumal@issp.ac.ru; Tel.: +7-916-6768673

Abstract: The study focused on a 21.99 at.%Ti–22.49 at.%Zr–20.35 at.%Hf–17.45 at.%Mo–17.73 at.%Cr). Analytical techniques such as X-ray diffraction, scanning electron microscopy as well as X-ray absorption spectroscopy were employed to investigate the alloy's structure, phase transformations, and properties. The alloy in the as-cast state contained three phases, namely the body-centred cubic (A2) phase, hexagonal Laves phase (C14), and cubic Laves phase (C15). The alloy has been annealed for a long time at different temperatures. It led to the disappearance of the hexagonal Laves phase, leaving behind two primary phases, namely the cubic Laves phase (C15) and the body-centered cubic phase (A2). At 1200 °C, the A2 phase almost disappeared, resulting in a practically single-phase sample. After a high-pressure torsion (HPT) treatment, the hexagonal Laves phase disappeared entirely, while the A2 and C15 phases remained. The grain size of the A2 and C15 phases was refined after HPT and grains were elongated, and their configuration resembled a layered structure. The high hardness of the A2 and C15 + C14 phases accounted this behavior. The lattice parameters in the A2 and C15 phases after HPT treatment approached those observed after prolonged annealing at 1000 °C, indicating that the composition of these phases after short-term high-pressure torsion at ambient temperature is equivalent to the composition of these phases after long tempering at 1000 °C. The rate of diffusion-like mass transfer during severe plastic deformation was estimated to be many orders of magnitude higher than that for conventional bulk diffusion at the HPT treatment temperature and similar to that at elevated temperatures above 1000 °C. X-ray absorption spectroscopy results obtained at K-edges of Ti, Cr, Zr, and Mo as well as at the L3-edge of Hf indicated that the local environment around metal atoms before HPT was similar to that after HPT. However, the static disorder increased after HPT, which could be attributed to an increased specific amount of metal atoms in the disordered grain boundary layers after HPT-driven grain refinement.

Keywords: high-entropy alloy; heat treatment; high-pressure torsion; Laves phases; solid solutions; XANES; EXAFS

1. Introduction

Since the high-entropy alloys (HEAs) were originally proposed by Cantor et al. [1] and Yeh et al. [2], there has been a growing interest in these multicomponent metallic materials. With a wide range of chemical compositions available, HEAs exhibit a variety of phase transformations, mechanical properties, and microstructural types, leading to a wealth of

research publications, including numerous reviews [3–6]. Typically, HEAs consist of five or more components, with proportions ranging from 5 to 35 at.%. Various methods were used to produce the HEAs. Especially promising are the HEAs in the form of coatings. Such HEA coatings were deposited with, for example, plasma cladding [7–14], plasma spray [15,16], thermal spray [17], laser cladding [18–20], magnetron sputtering [21–25], and vacuum arc deposition [26]. In many cases, HEAs exhibit a single-phase structure in a wide interval of temperatures, which consists of a multicomponent solid solution [27]. A key research goal is to clarify where are the borders of this single-phase region in terms of temperature and composition, as well as to explore ways to modify these boundaries.

Severe plastic deformation (SPD), such as high-pressure torsion (HPT) [28], is an important method for modifying the properties of HEAs. Several studies [29–35] have already been done to study the HPT influence on HEAs. HPT is particularly advantageous due to its ability to homogenize the sample processing, provided sufficient pressure and a number of plunger revolutions are used, as well as its ability to refine the grain structure. The grain refinement resulting from HPT can significantly increase the region of existence of a solid solution due to the segregation of components at the grain boundaries [36–39].

Here, we studied the HEAs which are similar to the alloys studied by Nagase et al. [40–44]. These HEAs were based on Ti and Zr with the addition of various combinations of other alloying elements: Ti–Zr–Hf–Cr–Mo and Ti–Zr–Hf–Co–Cr–Mo [40], Ti–Nb–Ta–Zr–Mo [41], Ti–Nb–Ta–Zr–X (X = V, Mo, W) [42], Ti–Nb–Ta–Zr–Mo [43], and Ti–Nb–Ta–Zr–Mo [44]. The HEA developed by Nagase et al. is a promising biomaterial for medical applications, including orthopedic implants [40]. This alloy showed good biocompatibility, comparable to commercial-grade titanium, as well as high Vickers hardness. The Ti–Zr–Hf–Mo–Cr HEA developed by Nagase et al. is a promising biomaterial for various medical applications, including orthopedic implants [40]. This alloy exhibits excellent biocompatibility comparable to that of commercially available titanium, in addition to a high Vickers hardness, making it a promising candidate for implant materials.

In our study, we aimed to investigate the impact of annealings and HPT on the microstructure and phase transitions of the TiZrHfCrMo alloy, which holds great promise for medical applications such as orthopedic implants. Given its potential use in medical devices, it is essential to understand how to control its phase transformations and mechanical properties under different heat treatment conditions. In contrast to the method employed in Ref. [42], we used levitational melting in a pure argon atmosphere to manufacture the TiZrHfCrMo alloy ingot.

X-ray absorption spectroscopy (XAS) was employed to study the local atomic structure of the HEAs before and after HPT treatment. Due to its element selectivity, XAS is well-suited for studying multicomponent compounds such as HEAs, as it delivers data on the local environment surrounding an atom of a specific element [45]. However, the complex configurational and chemical disorder inherent in HEAs poses a challenge in extracting structural information, as it requires a model that depends on a multitude of parameters.

2. Experimental Section

The high-entropy alloy TiZrHfMoCr, consisting of 11.35 wt.%Ti, 22.09 wt.%Zr, 38.91 wt.%Hf, 17.80 wt.%Mo, and 9.85 wt.%Cr (or 21.99 at.%Ti, 22.49 at.%Zr, 20.35 at.%Hf, 17.45 at.%Mo, and 17.73 at.%Cr), was prepared by melting pure metals in the atmosphere of pure argon in the induction furnace. The alloy was then cast into a cylindrical ingot. It has a diameter of 10 mm. Pure metals have been used such as titanium grade TI-1 (99.98 wt.% iodide titanium), zirconium (99.98 wt.% iodide zirconium), hafnium (99.95 wt.% iodide hafnium), molybdenum (99.97 wt.%), and chromium (99.99 wt.%). The ingot was cut into 0.8 mm thick discs using spark erosion (Electroerosive Wire Machine with NPC System, Model: DK7735, Suzhou LongkaiElectromechenical Technology CO, LTD., Suzhou, China). The surface-hardened layer was removed using the grinding paper with a roughness of 68 μm. Then the samples were put in the evacuated quartz ampoules and annealed in the resistance furnace. The residual pressure in the ampoules was about 7.5×10^{-3} Pa.

To investigate the influence of heat treatment on structure and properties, the discs were annealed at different temperatures and durations: 600 °C for 480 h, 800 °C for 336 h, 1000 °C for 24 and 336 h, 1200 °C for 144 h, and in SNOL 6.7/1300 furnaces. Two discs of the initial alloy were subjected to HPT in the installation with computer control (W. Klement GmbH, Lang, Austria) at 7 GPa, with an anvil rotation speed of 1 rpm for 5 rotations. The thickness of the samples after HPT treatment was reduced to 0.35 mm. After HPT, one of the samples was annealed at 1000 °C (96 h). The samples were polished with diamond paste before SEM studies (grain size of 1 μm).

Elemental analysis was conducted on an FEI Dual Beam Versa 3D HighVac scanning electron microscope (SEM) manufactured by FEI (Hillsboro, OR, USA). X-ray diffraction (XRD) patterns were collected using a Siemens D-500 X-ray diffractometer (Munich, Germany) equipped with a copper anode (Cu-Kα radiation) tube to perform structural-phase analysis of the samples. PowderCell 2.4 program (PowderCell for Windows. Version 2.4. 03.08.2000, Werner Kraus & Gert Nolze, BAM, Berlin, Germany) was utilized for phase analysis and calculation of lattice parameters.

The X-ray absorption spectroscopy experiments were performed at the synchrotron radiation facility DESY PETRA-III in Hamburg, Germany. The P65 Applied XAFS undulator beamline's experimental setup was used [46]. The setup included a fixed exit Si(111) double-crystal monochromator and uncoated as well as Rh-coated silicon plane mirrors for harmonic reduction. X-ray absorption spectra were measured at room temperature at the K-edges of Ti, Cr, Zr, and Mo, as well as the L_3-edge of Hf in fluorescence mode. Two detectors were used: an ionization chamber (I_0) to measure the incident radiation located before the sample, and a passivated implanted planar silicon (PIPS) detector (I_f) positioned at 90° to the incident beam to collect X-ray fluorescence from the sample. The size of the X-ray beam at the sample was 2.5×0.3 mm^2. X-ray absorption coefficients were obtained using the formula $\mu(E) = I_f/I_0$, where I_f is the intensity of the fluorescence signal from the sample and I_0 is the intensity of the incident beam measured by an ionization chamber located before the sample. The EXAFS (extended X-ray absorption fine structure) spectra and XANES (X-ray absorption near-edge structure) spectra have been analyzed with the aid of the XAESA code [47]. The required phase functions and backscattering amplitude were calculated. For this purpose, the ab initio self-consistent real-space multiple-scattering FEFF8.50L code was used [48,49]. The EXAFS contributions from the first coordination shells of the five metals were analyzed using either the single-scattering cumulant approximation or the regularization technique [50], following a conventional procedure.

3. Results Together with Discussion

The SEM (Figure 1a,b) and XRD analysis (Figure 1c) were carried out to characterize the as-cast TiZrHfMoCr alloy ingot. Table 1 contains the results of the elemental analysis. The alloy comprises five components, and its microstructure reveals three regions with varying gray gradations attributed to the different chemical compositions (Figure 1b).

By establishing a correlation between the chemical composition, the color gradation in the micrographs, and the phases identified from the XRD patterns, we were able to determine that the light gray area (1) corresponds to the body-centered cubic (bcc) phase (A2), which is rich in hafnium, molybdenum, and zirconium (Im-3m). The dark gray region (2) corresponds to the cubic (C15) Laves phase (Fd-3m), while the gray region (3) corresponds to the hexagonal (C14) Laves phase (P63/mmc).

Table 1. Composition of the TiZrHfMoCr sample measured in different points (see Figure 1b), wt.%.

Point	Phase	Ti	Cr	Zr	Mo	Hf
1	(Hf)cub (A2)	6.3 ± 0.1	12.8 ± 0.1	13.0 ± 0.2	29.4 ± 0.3	38.5 ± 0.3
2	$(Mo,Cr)_2Zr$ (C15)	12.4 ± 1.9	10.3 ± 1.1	24.9 ± 1.6	15.1 ± 2.1	38.6 ± 0.6
3	Cr_2Zr (C14)	14.6 ± 0.9	7.9 ± 0.9	28.2 ± 1.2	11.1 ± 0.9	39.5 ± 0.6
	Average composition	11.3	9.9	22.1	17.8	38.9
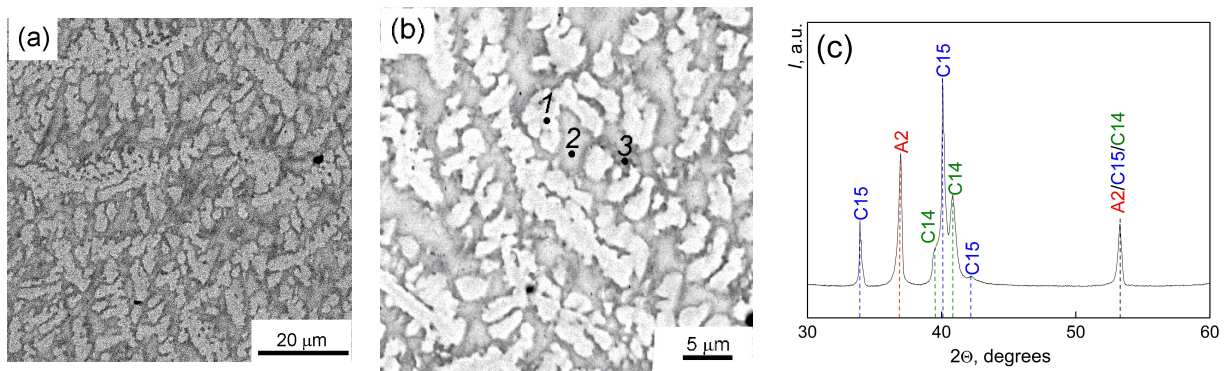
Figure 1. SEM images of the initial microstructure of the TiZrHfMoCr alloy: (**a**) general view, (**b**) dots mark the areas of component analysis: light gray (1), dark gray (2), and gray (3) colors. (**c**) X-ray diffraction pattern of the as-cast TiZrHfMoCr alloy.

After annealing at 1000 °C for 24 h, the morphology of the structural components and the phase composition changed significantly. It can be seen in Figure 2a,b, respectively. Notably, one of the Laves phases (C14) vanished. The X-ray diffraction analysis of the annealed sample revealed the presence of two phases: the C15 Laves phase and the A2 bcc phase, with a phase ratio of approximately 70/30 (Figure 2a). Table 2 contains the results of the XRD analysis.
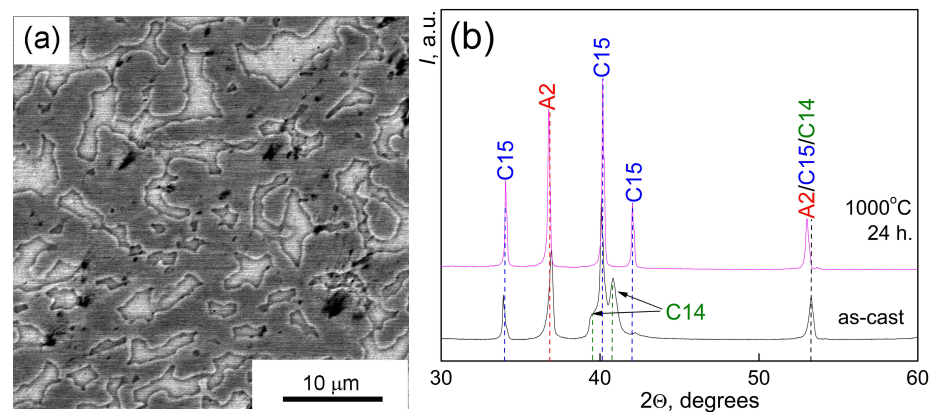
Figure 2. Characteristics of the TiZrHfMoCr alloy annealed at 1000 °C for 24 h. (**a**) SEM micrograph, (**b**) XRD patterns of the TiZrHfMoCr alloy in the original as-cast state (black line, bottom) and after annealing (pink line, top).

Table 2. Phases, lattice parameters *a*, *c* of phases, the volume fraction of phases *V* in the TiZrHfMoCr alloy in the initial as-cast state and annealed state (1000 °C, 24 h).

Phase	Initial Alloy		1000 °C 24 h	
	a, c, nm	V, %	a, nm	V, %
(A2)	0.3435	35	0.3452	30
(C15)	0.7451	45	0.7436	70
(C14)	0.5249; 0.8656	20	-	-

We conducted a series of annealing treatments for a prolonged duration (144–480 h) at various temperatures ranging from 600 to 1200 °C, to achieve an equilibrium state (as depicted in Figure 3a–d). The corresponding XRD patterns are illustrated in Figure 3e, and their analysis is presented in Table 3. The phase nomenclature in Table 3 uses (B1) for the face-centered cubic (fcc) phase, $(HfC)_{cub}$, and (C36) for the phase $(Cr_2Hf)_{hex}$. With increasing annealing temperature, the microstructure of the annealed alloys (Figure 3a–d) exhibited a significant change, and the size of the individual grains of all phases increased

with increasing annealing temperature. It is worth mentioning that at 1200 °C about 6% of the volume consisted of a combination of oxides, nitrides, and carbides (Ti$_2$O$_3$, Cr$_2$N, HfC). The sample after annealing was heavily deformed and oxidized. In Figure 3d, three distinct regions with different shades are visible and labeled as (1), (2), and (3).

It has to be underlined that the prolonged heat treatment at 1000 °C (24 to 336 h) brought about significant changes in the volume fraction of the phases. As shown in Figures 2b and 3e, the (A2) phase nearly disappeared, and the sample became almost single-phase, comprising mainly the Laves phase (C15). After annealing at 1200 °C, the XRD peak of the bcc A2 phase was slightly higher than that at 1000 °C, indicating a volume fraction of approximately 5% for the A2 phase. Additionally, small amounts of the fcc phase (B1) and the Laves phase (C15-2) with increased lattice parameter $a = 0.7416$ nm also emerged, as revealed by the XRD patterns.
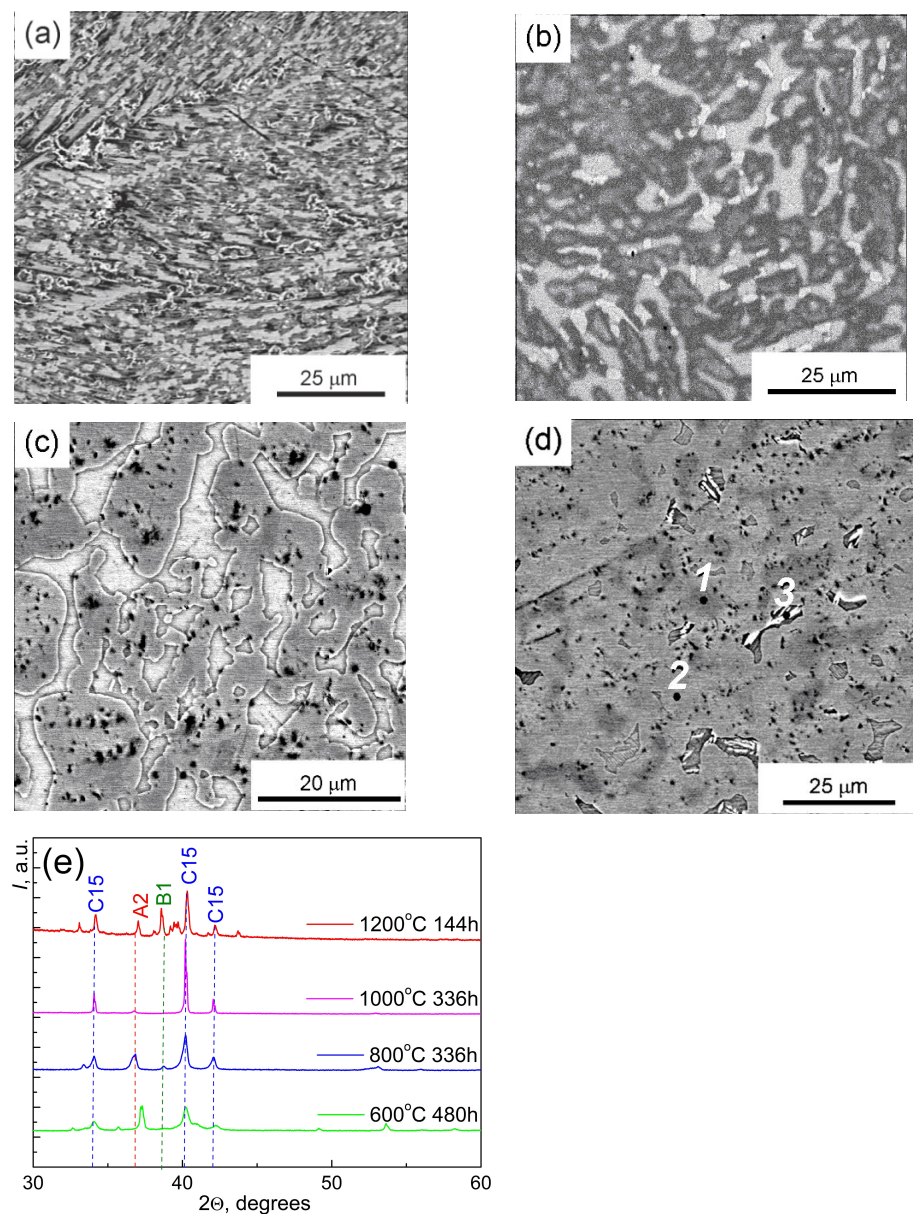

Figure 3. SEM micrographs of a TiZrHfMoCr alloy annealed at (**a**) 600 °C, 480 h, (**b**) 800 °C, 336 h, (**c**) 1000 °C, 336 h, (**d**) 1200 °C, 336 h and (**e**) diffraction patterns for annealed alloys: 1200 °C, 336 h (red line), 1000 °C, 480 h (pink line), 800 °C, 144 h. (blue line) and 600 °C, 480 h (green line).

Table 3. Phases, lattice parameters *a, c* of phases, and the volume fraction *V* of phases in the TiZrHfMoCr alloy after annealings at different temperatures.

Phase	600 °C 480 h		800 °C 336 h		1000 °C 336 h		1200 °C 144 h	
	a, c, ʜᴍ	**V, %**	**a,** ʜᴍ	**V, %**	**a,** ʜᴍ	**V, %**	**a,** ʜᴍ	**V, %**
(A2)	0.3417	45	0.3445	25	0.3464	2	0.3429	5
(C15)	0.7424	45	0.7431	70	0.7453	98	0.7416	90
(C15-2)	-	-	-	-	-	-	0.7621	3
(B1)	-	-	0.4642	5	-	-	0.4656	2
(C36)	0.5021; 0.6438	10	-	-	-	-	-	-

Between 600 to 1000 °C, there is a slight increase in the lattice parameters of phases (C15) and (A2), followed by a subsequent decrease when the temperature is increased from 1000 to 1200 °C (Figure 4). It is noteworthy that the lattice parameters of the (C15) and (A2) phases in the as-cast sample approximately align with the lattice parameters of these phases at annealing temperatures between 800 and 1000 °C (Figure 4).
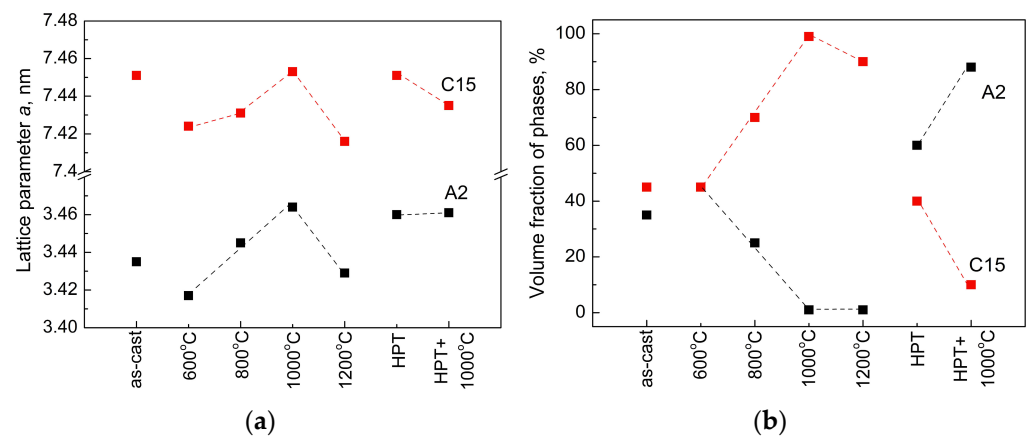
Figure 4. Changes in (**a**) lattice parameters and (**b**) the volume fraction of phases (A2) and (C15) in the original sample, after anneals at 600, 800, 1000, and 1200 °C, after HPT, and after HPT with additional annealing at 1000 °C.
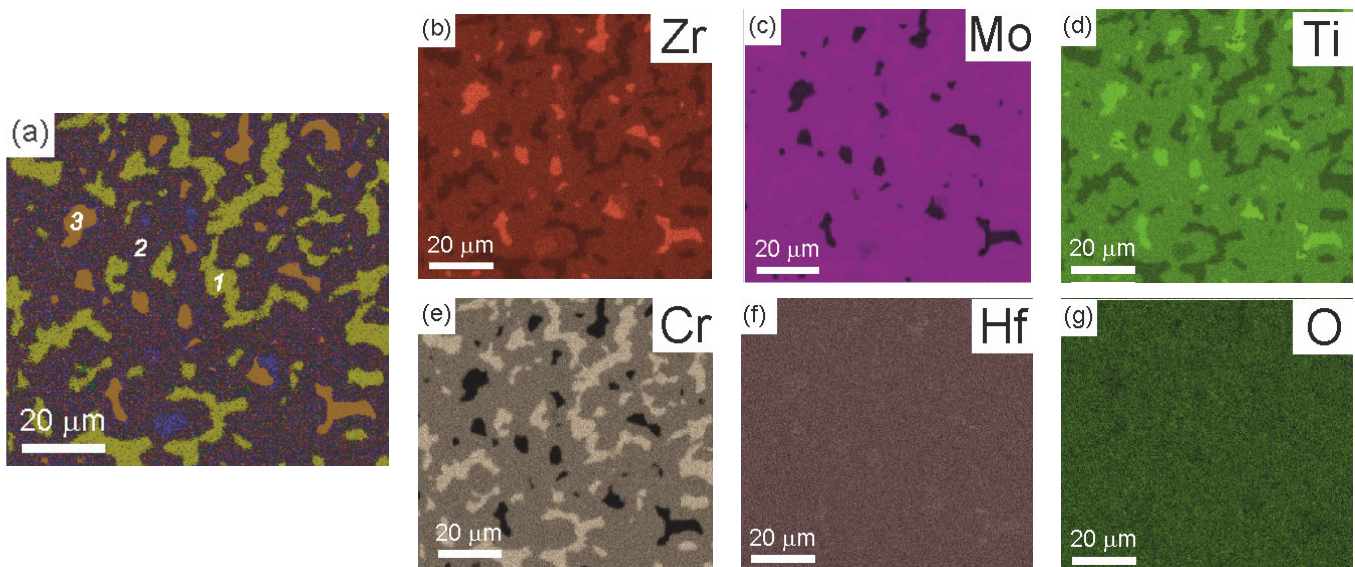
We conducted a chemical analysis of three regions (labeled as 1, 2, and 3 in Figure 5a) in a sample annealed at 1200 °C and determined their composition. Region 1 exhibited an enrichment of zirconium, molybdenum, and chromium in the ratio of Zr14-Mo24-Cr19 (wt.%). Region 2 showed the enrichment of titanium, zirconium, molybdenum, and chromium in the ratio of Ti13-Zr20-Mo20-Cr12. Region 3 displayed the enrichment of titanium and zirconium in the ratio of Ti18-Zr37. The hafnium was found to be uniformly distributed throughout the sample, with a concentration of 35 ± 3 wt.% in all structural components. Additionally, the sample was found to contain approximately 2 wt.% of oxygen, although the impact of oxygen on phase transformations was not studied in this work.

Based on the chemical analysis data, we were able to identify the region (1) as the (A2) phase, region (2) as the (C15) phase, and region (3) as the (B1) phase (Table 4). It is apparent that the (A2) phase partially or completely encloses the grains of the C15 phase, suggesting that the second solid phase (A2) is "wetting" the C15/C15 grain boundaries.

In the subsequent step, we subjected the initial cast sample to HPT deformation. A comparison of diffraction patterns between the as-cast sample before HPT and the sample after HPT (Figure 6a) reveals a significant broadening of the diffraction peaks, similar to what we have previously observed for various binary titanium alloys [51–54]. This broadening suggests a reduction in grain size to the range of 150–200 nm. Upon comparing the SEM micrographs of the sample before and after HPT (Figures 1a,b and 6a, Table 5), we observed that the sample still exhibited alternating light and dark areas that corresponded to

phases (A2) and (C15). These regions only slightly stretched in the direction of deformation. The width and length of these regions were approximately 2–3 μm and 10 μm, respectively. This suggests that grain refinement occurred within the regions (A2) and (C15) while maintaining their original shape, and the mixing of the phases (A2) and (C15) did not occur. We observed this phenomenon in the systems where the hardness of constituent phases is high [55–57]. In such cases, the areas occupied by the phases remained almost unchanged in shape during HPT, and grain refinement occurred separately within each phase.

Before undergoing HPT treatment, the sample consisted of three phases: the (C14) Laves phase, the (C15) Laves phase, and the (A2) bcc phase. Following HPT, the Laves phase (C14) disappeared, while the volume fraction of the (C15) Laves phase remained almost unchanged. The volume fraction of the (A2) bcc phase, however, increased to 60% from 45% (Table 4). Additionally, there was an important lattice parameter change of the (A2) and (C15) phases compared to the initial as-cast state before HPT (Figure 4, Tables 2 and 4). After HPT, the lattice parameters of the (A2) and (C15) phases were similar to the lattice parameters of these phases in the sample annealed at 1000 °C for a long time. This similarity in lattice parameters between the sample after HPT and the sample annealed at 1000 °C allows us to compare these findings with HPT experiments where the decomposition of a solid solution was in competition with its formation [57,58]. These results allowed us to determine the value of T_{eff} called effective temperature. In these experiments, a certain concentration of the diluted component in the solid solution was established after HPT, which was equal to its solubility at some elevated temperature. We refer to this temperature as the effective temperature T_{eff}. Therefore, HPT at room temperature and short treatment time resulted in the dilution of a second component, which can be reached by long-term annealing at an elevated temperature T_{eff}. Thus, we can cautiously conclude that the HPT of the TiZrHfMoCr high-entropy alloy is equivalent to its long-term annealing at an (effective) temperature of 1000 °C.


Figure 5. Chart of the chemical analysis of the sample shown in Figure 3d (after annealing at 1200 °C, 144 h). (**a**) General view with the main three regions differing in composition. Region 1 is enriched on Zr, Mo, Cr. Region 2 is enriched on Ti, Zr, Mo, Cr. Region 3 is enriched on Ti, Zr (see more detailed explanations in text). (**b–g**) Element distribution map.

Table 4. Composition of individual regions (1–3) of the TiZrHfMoCr alloy, presented in wt.%.

Point	Phase	Ti	Cr	Zr	Mo	Hf
1	(A2)	8.18	19.15	14.16	24.73	33.78
2	(C15)	12.70	12.03	20.77	20.08	34.42
3	(B1)	18.35	1.26	37.95	5.15	37.29
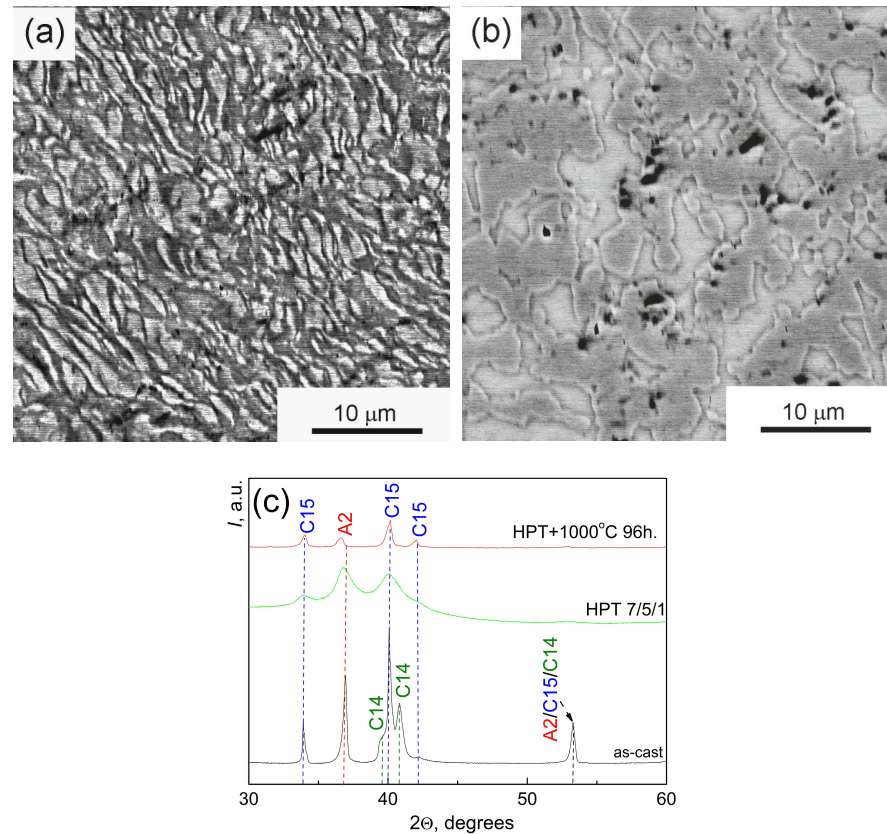
Figure 6. SEM micrographs of the TiZrHfMoCr alloy after high-pressure torsion: (**a**) the as-cast sample subjected to high-pressure torsion, (**b**) high-pressure torsion and additional annealing at 1000 °C, 96 h. (**c**) Diffraction patterns of the initial sample (black line), after HPT (green line) and after high-pressure torsion plus annealing at 1000 °C, 96 h. (red line).

Table 5. Phases, lattice parameters *a*, *c* of phases, the volume fraction *V* for the phases in TiZrHfMoCr alloy in the initial state, after high-pressure torsion and after high-pressure torsion with additional annealing at 1000 °C.

| Phase	As-Cast Alloy		High-Pressure Torsion		High Pressure Torsion + 1000 °C 96 h	
	a, c, nm	V, %	a, нм	V, %	a, нм	V, %
(A2)	0.3435	35	0.3460	60	0.3461	40
(C15)	0.7451	45	0.7451	40	0.7435	60
(C14)	0.5249; 0.8656	20	-	-	-	-

The changes in the composition of the constituent phases during HPT occur due to diffusion-like mass transfer. One can estimate the rate of mass transfer using the relation $L = (Dt)^{0.5}$, which relates the length of the diffusion path *L*, bulk diffusion coefficient *D*, and the HPT treatment time *t*. In this study, the treatment time was *t* = 300 s and *L* can be estimated as grain size after HPT *L* = 200 nm. This yields a bulk self-diffusion coefficient for mass transfer which is diffusion-like and driven by the HPT as $D \sim 10^{-16}$ m^2/s. Comparatively, the bulk self-diffusion coefficients for the constituent elements in our HEA

at room temperature range from 10^{-30}–10^{-40} m/s for Ti [59,60], Zr [61–66], Hf [67–69], Mo [70,71], and Cr [72,73]. Therefore, HPT significantly increases the rate of diffusion-like mass transfer, consistent with our observations in Cu- and Al-based alloys [58,74]. It contradicts the fact that high pressure alone (beyond shear strain) decreases the rate of diffusion-controlled processes [75–77]. Moreover, the value of $D \sim 10^{-16}$ m^2/s for the bulk self-diffusion coefficient is comparable to that observed at elevated temperatures of 900–2000 °C for Ti [59,60], Zr [61–66], Hf [67–69], Mo [70,71], and Cr [72,73]. In other words, the D value for the diffusion-like mass transfer driven by the high-pressure torsion is comparable to the bulk self-diffusion coefficient in constituent elements of our HEA at the increased temperature of 900–2000 °C. Here we can remember that the phases after HPT are as if the sample was annealed at T_{eff} of 1000 °C. This means that the phase composition and the mass transfer rate indicate that the structure and properties of HEA at steady-state HPT are similar to those at elevated temperatures.

However, we have to underline that the volume fractions of phases (A2) and (C15) after HPT show significant differences compared to those after annealing at 1000 °C. While the sample becomes almost single-phase and consists mainly of one Laves phase (C15) after annealing at 1000 °C, the volume fractions of the (A2) and (C15) phases are comparable to each other after HPT (Table 4). Further annealing of the HPT-treated sample at 1000 °C reduces the width of the XRD diffraction peaks (Figure 6c), indicating grain growth. However, the grain size does not reach that of the as-cast sample. Additionally, the volume fraction of the (A2) phase slightly goes down after the additional annealing, suggesting that the sample is gradually approaching the state of the original cast sample after long-term annealing (Table 3).

As we have shown above, the shape of the regions where the (A2) and (C15) phases are located undergoes little change after HPT, as seen in Figures 1a,b and 6a. This is attributed to the hardness of the phases (A2) and (C15), which maintain their shapes during the HPT process. To confirm this hypothesis, we measured the value (E) being the Young's modulus and (H) being the nanohardness across the original as-cast sample, as shown in Figure 7. Although only two phases, namely light and dark ones, were visually distinguished in an optical microscope, we designated them as (A2) and (C15 + C14) based on the P-h diagrams in Figure 7a. The average H and E values were calculated for each phase. The results indicate that there is an insignificant difference in both H and E between the (A2) and (C15 + C14) phases, with H_{middle} values of 8.2 ± 1.4 GPa and 8.0 ± 1.9 GPa, and E_{middle} values of 123 ± 5 GPa and 122 ± 10 GPa, respectively.
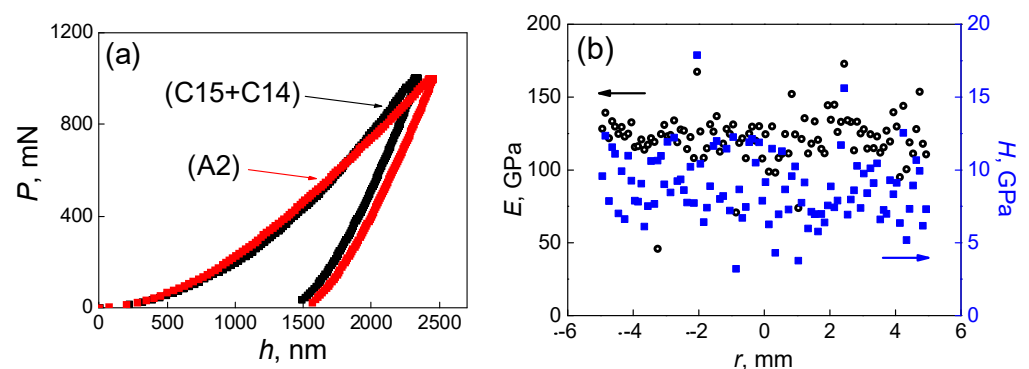
Figure 7. Measurements of nanohardness H and Young's modulus E for the original as-cast TiZrHfMoCr alloy. (**a**) P-h diagrams taken from (A2) area (red symbols) and (C15 + C14) area (black symbols). (**b**) Dependences of H and E measured across the initial alloy sample.

Using the X-ray absorption spectroscopy at the K-edges of Ti, Cr, Zr, Mo, and L$_3$-edge of Hf, we analyzed the local atomic structure of TiZrHfMoCr HEAs in both the as-cast (AC) and high-pressure torsion treated (HPT) samples. The normalized X-ray absorption near-edge structure (XANES) spectra of the HEAs are presented in Figure 8, which demonstrate

the similarity of the local environment around metal atoms before and after HPT. The K-edge XANES spectra display a pre-edge peak/shoulder A arising from the 1s → nd (n = 3 for Ti and Cr, n = 4 for Zr and Mo) transition [78,79], which becomes less prominent at higher excitation energies due to an increase in the natural line width of the 1s core level for heavier elements [80]. At the Hf L_3-edge, the strong resonance just above the edge, known as the white line (WL), is produced by the dipole-allowed transition $2p_{3/2}$(Hf) → 5d [81].
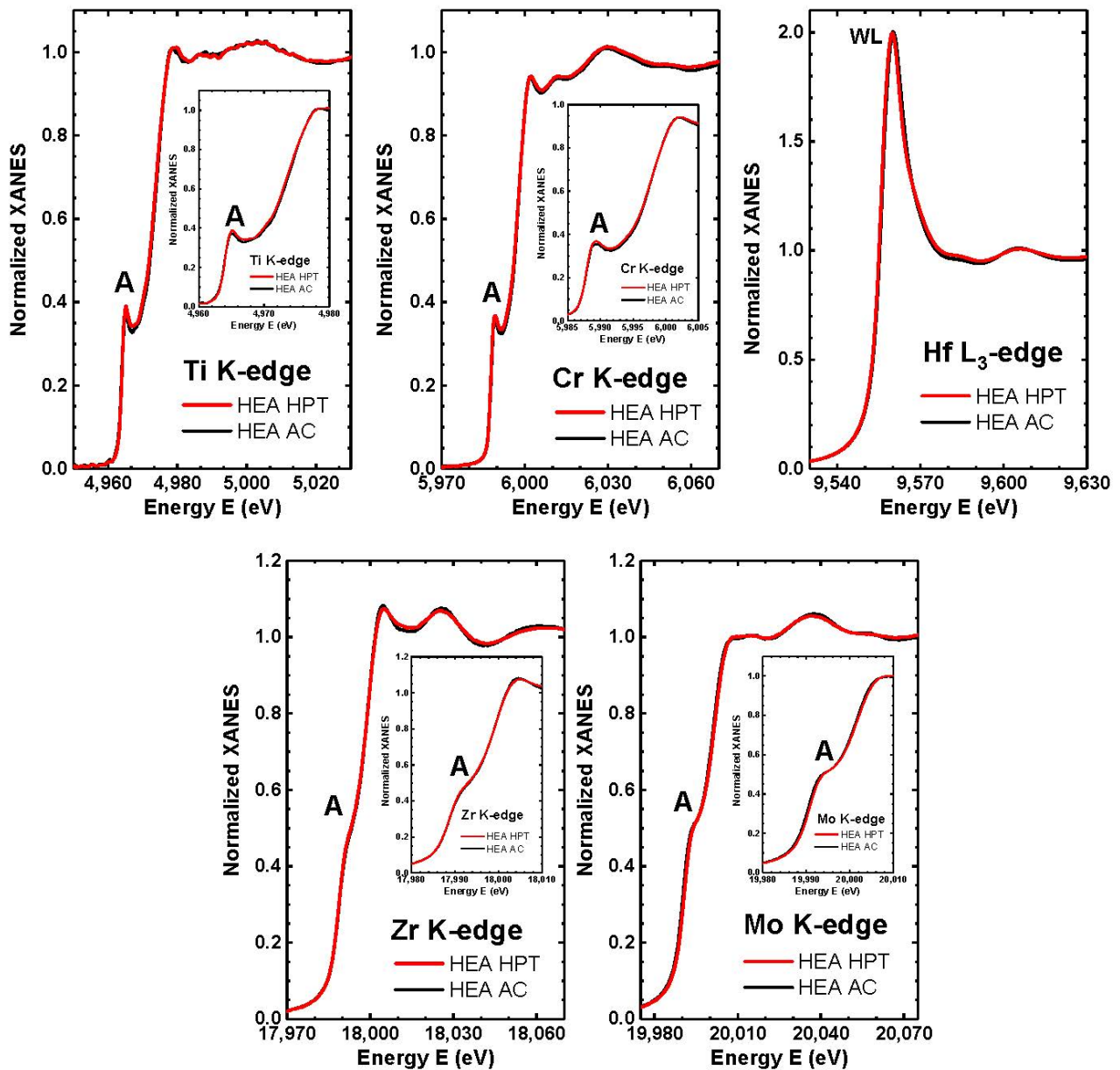
Figure 8. XANES spectra of the original as-cast (AC) TiZrHfMoCr HEA sample and sample after HPT at the Ti, Cr, Zr, and Mo K-edges and Hf L_3-edge. The insets show an enlarged view around the edge. The pre-edge A and the white line WL are indicated.

The experimental extended X-ray absorption fine structure (EXAFS) spectra $\chi(k)k^2$ (where k is the photoelectron wavenumber [48]), are depicted in Figure 9. Notably, the shape of the EXAFS spectra remains largely unchanged after HPT, indicating that the local environment around metal atoms is generally preserved. However, at large k-values, the EXAFS oscillations for the Cr, Zr, Mo, and Hf absorption edges become dampened, indicating an increase in static disorder. This increase in static disorder can be attributed

to the higher specific area of grain boundaries resulting from strong grain refinement during HPT.
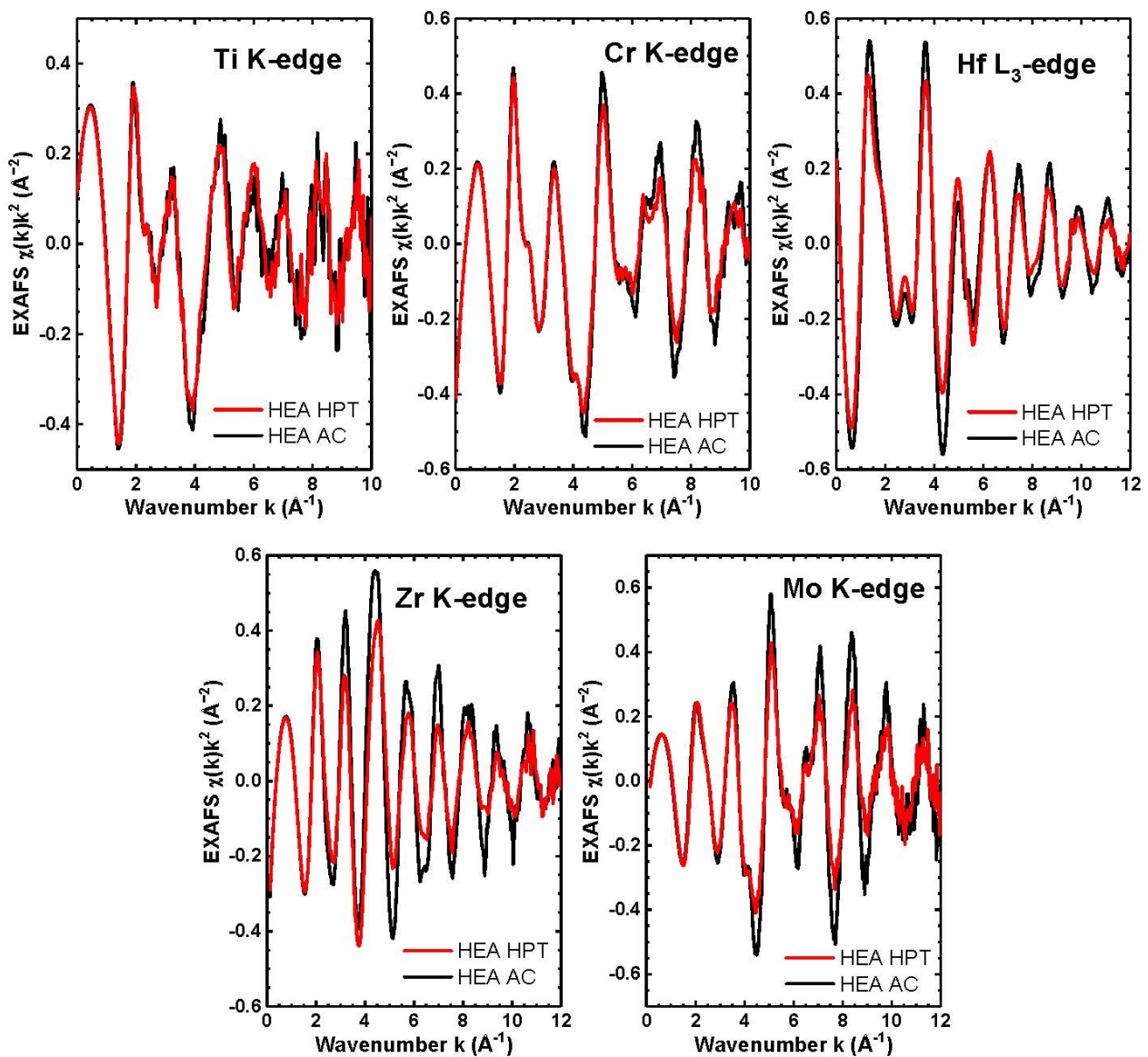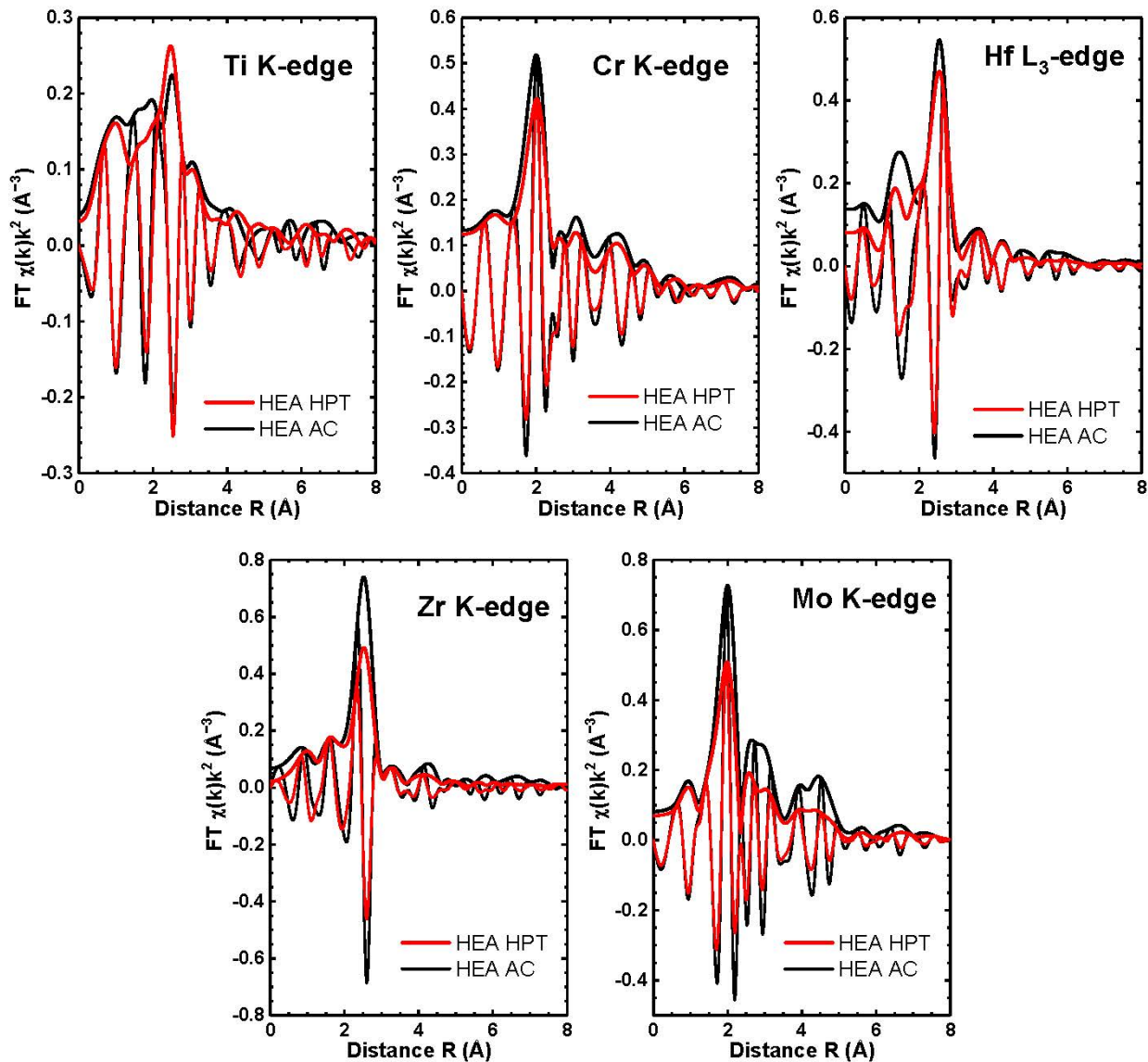

Figure 9. EXAFS spectra of as-cast TiZrHfMoCr HEA sample (AC) and sample after HPT at the Ti, Cr, Zr, and Mo K-edges and Hf L_3-edge.

The Fourier transforms (FTs) of the EXAFS spectra are presented in Figure 10 and indicate that the most significant alterations due to high-pressure torsion are observed around Zr and Mo atoms. We have to underline that the peaks in the FTs are shifted approximately 0.5 Å to smaller distances relative to their crystallographic values, which is due to the shift of the backscattering phase in the formula for EXAFS [48].

The FTs were subjected to a more detailed comparison in Figure 11, allowing us to discern three distinct local environments in the HEAs. The FT maximum corresponding to the nearest group of atoms is located at about 0.4 Å shorter distances for Mo and Cr than for Zr and Hf. However, no well-defined peak was found in the FT at the K-edge of titanium, indicating that Ti atoms occupy a strongly broadened or multi-site environment. The analysis of the EXAFS spectra obtained using a beam spot size of 0.75 mm^2 was challenging due to the multi-phase nature of the samples (Table 1). Nonetheless, we roughly estimated the effective radius of the first coordination shell of metal atoms from the frequency of the EXAFS component responsible for the main peak in the FTs. To ensure the credibility of

our estimate, we employed two simulation methods, namely the cumulant approach and the regularization technique [48]. It should be noted that due to the possibility of atoms of different types being present in the first coordination shell of a particular metal and the potential for metal atoms to occupy crystallographically distinct sites with varying degrees of distortion, only estimates for the values of interatomic distances can be made.


Figure 10. Fourier transforms (modulus and imaginary parts) of the EXAFS spectra for as-cast sample (AC) and sample after HPT of TiZrHfMoCr HEAs at the Ti, Cr, Zr, and Mo K-edges and Hf L_3-edge.

We discovered that the first shell radius was approximately 2.6–2.7 Å for Mo and Cr, and around 3.0–3.1 Å for Zr and Hf. In contrast, the distribution of the nearest atoms around Ti was much wider, ranging from 2.5 to 3.1 Å. These values can be compared to the crystallographic distances in the as-cast HEA, which were calculated based on the lattice parameters in Table 2 for the three phases reported in Table 1. The first shell radius in the two Laves phases, C14 and C15, was around 2.6–2.7 Å for Cr and roughly 3.1 Å for Zr, which agrees with our expectations from the EXAFS results. Similarly, the first shell radius for Hf in the A2 phase was approximately 3.0 Å, and its value should be about 3.1 Å when Hf substitutes Zr in Laves phases, which is also in agreement with the EXAFS findings. The first shell radius for Mo corresponded to its preferred location at the Cr sites, as observed in the C15 phase. Finally, the metallic radius of titanium atoms (1.47 Å) was higher than the

radii of Cr (1.28 Å) as well as Mo (1.39 Å) but smaller than the radii of Hf (1.59 Å) and Zr (1.60 Å). Therefore, when Ti atoms were present at both positions, it should be accompanied by local structural relaxation, which was indeed observed in the EXAFS.
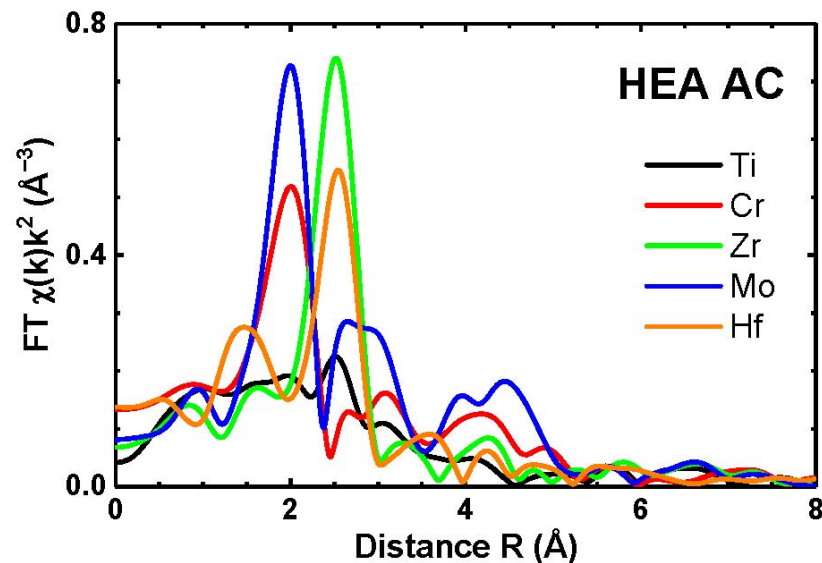
Figure 11. Comparison of the Fourier transform of the EXAFS spectra for as-cast (AC) TiZrHfMoCr HEA at the K-edges of Ti, Cr, Zr, and Mo and L_3-edge of Hf. Only the moduli of FTs are shown for clarity.

4. Conclusions

The structure, phase transformations, and properties of the 21.99 at.%Ti–22.49 at.%Zr–20.35 at.%Hf–17.45 at.%Mo–17.73 at.%Cr high-entropy alloy were investigated in various states, including the initial as-cast state, after annealing, after high-pressure torsion (HPT) treatment, and after additional annealing. The investigation employed various methods, such as X-ray diffraction, scanning electron microscopy, and X-ray absorption spectroscopy.

In its initial as-cast state, the HEA comprised three phases: the body-centered cubic phase A2, the cubic C15 Laves phase, and the hexagonal C14 Laves phase. Upon annealing between 600 and 1200 °C, only the (A2) and (C15) phases remained in the samples. After subsequent HPT treatment, the significant grain refinement of the (A2) and (C15) phases took place, and the (C14) phase completely disappeared. Nevertheless, the shape of the initial regions occupied by the (A2) and (C15) phases remained mostly intact during HPT, indicating that these phases were not intermixed, and the grains were refined and elongated separately within each phase.

HPT changed the lattice parameters of the (A2) and (C15) phases, bringing them closer to the values observed after prolonged anneal at 1000 °C. Therefore, the composition of the (A2) and (C15) phases after short-term HPT deformation at room temperature is similar to the composition in the sample annealed a long time at 1000 °C. The rate of diffusion-like mass transfer estimated during severe plastic deformation is many orders of magnitude higher than that observed for usual diffusion in the volume at the temperature of HPT treatment. It is comparable to that observed at elevated temperatures above 1000 °C.

An intriguing phenomenon was observed when HPT was followed by short annealing at 1000 °C: while the lattice parameters did not change and no additional phases appeared (as was in the case with annealing alone), the ratio of the (A2) and (C15) phase fractions changed in a mirrored fashion. This suggests that it is possible to manipulate the phase ratio by using a combination of HPT and annealing of different durations.

Finally, the X-ray absorption spectroscopy results obtained at the K-edges of Ti, Cr, Zr, Mo, and L_3-edge of Hf demonstrate that the local arrangement of metal atoms is preserved after HPT treatment, except for some increased static disorder, presumably in the grain boundary region. Nonetheless, distinct local environments around Mo/Cr, Zr/Hf, and

Ti atoms were identified. These metal atom sites, obtained from EXAFS analysis, are consistent with the crystallographic phases identified by X-ray diffraction.

Author Contributions: Conceptualization, A.K. and B.S.; methodology, A.G., A.D. and G.D.; formal analysis, N.A. and A.T.; writing—original draft preparation, A.G., A.D. and E.C.; writing—review and editing, N.A., B.S. and A.K.; supervision, B.S. and A.K.; project administration, N.A. and B.S.; funding acquisition, A.D. and B.S. All authors have read and agreed to the published version of the manuscript.

Institutional Review Board Statement: Not applicable.

Informed Consent Statement: Not applicable.

Data Availability Statement: Data are contained within the article.

Conflicts of Interest: The authors declare no conflict of interest. The funders had no role in the design of the study; in the collection, analyses or interpretation of data; in the writing of the manuscript or in the decision to publish the results.

References

1. Cantor, B.; Chang, I.T.H.; Knight, P.; Vincent, A.J.B. Microstructural development in equiatomic multicomponent alloys. *Mater. Sci. Eng. A* **2004**, *375–377*, 213–218. [CrossRef]
2. Yeh, J.-W.; Chen, S.K.; Lin, S.-J.; Gan, J.-Y.; Chin, T.-S.; Shun, T.-T.; Tsau, C.-H.; Chang, S.-Y. Nanostructured High-Entropy Alloys with Multiple Principal Elements: Novel Alloy Design Concepts and Outcomes. *Adv. Eng. Mater.* **2004**, *6*, 299–303. [CrossRef]
3. Zhang, Y.; Zuo, T.T.; Tang, Z.; Gao, M.C.; Dahmen, K.A.; Liaw, P.K.; Lu, Z.P. Microstructures and properties of high-entropy alloys. *Prog. Mater. Sci.* **2014**, *61*, 1–93. [CrossRef]
4. Straumal, B.B.; Klinger, L.; Kuzmin, A.; Lopez, G.A.; Korneva, A.; Straumal, A.B.; Vershinin, N.; Gornakova, A.S. High Entropy Alloys Coatings Deposited by Laser Cladding: A Review of Grain Boundary Wetting Phenomena. *Coatings* **2022**, *12*, 343. [CrossRef]
5. Straumal, B.; Korneva, A.; Kuzmin, A.; Klinger, L.; Lopez, G.A.; Vershinin, N.; Straumal, A.; Gornakova, A. High Entropy Alloys for Energy Conversion and Storage: A Review of Grain Boundary Wetting Phenomena. *Energies* **2022**, *15*, 7130. [CrossRef]
6. Straumal, B.; Rabkin, E.; Lopez, G.A.; Korneva, A.; Kuzmin, A.; Gornakova, A.; Straumal, A.; Baretzky, B. Grain Boundary Wetting Phenomena in High Entropy Alloys Containing Nitrides, Carbides, Borides, Silicides, and Hydrogen: A Review. *Crystals* **2021**, *11*, 1540. [CrossRef]
7. Amiri, A.; Shahbazian-Yassar, R. Recent progress of high-entropy materials for energy storage and conversion. *J. Mater. Chem. A* **2021**, *9*, 782–823. [CrossRef]
8. Liu, H.; Syama, L.; Zhang, L.; Lee, C.; Liu, C.; Dai, Z.; Yan, Q. High-entropy alloys and compounds for electrocatalytic energy conversion applications. *Susmat* **2021**, *1*, 482–505. [CrossRef]
9. Gao, P.-H.; Fu, R.-T.; Chen, B.-Y.; Zeng, S.-C.; Zhang, B.; Yang, Z.; Guo, Y.-C.; Liang, M.-X.; Li, J.-P.; Lu, Y.-Q.; et al. Corrosion Resistance of CoCrFeNiMn High Entropy Alloy Coating Prepared through Plasma Transfer Arc Claddings. *Metals* **2021**, *11*, 1876. [CrossRef]
10. Wang, M.; Lu, Y.; Zhang, G.; Cui, H.; Xu, D.; Wei, N.; Li, T. A novel high-entropy alloy composite coating with core-shell structures prepared by plasma cladding. *Vacuum* **2021**, *184*, 109905. [CrossRef]
11. Zhang, D.; Yu, Y.; Feng, X.; Tian, Z.; Song, R. Thermal barrier coatings with high-entropy oxide as a top coat. *Ceram. Int.* **2022**, *48*, 1349–1359. [CrossRef]
12. Wang, L.; Zhang, F.; Yan, S.; Yu, G.; Chen, J.; He, J.; Yin, F. Microstructure evolution and mechanical properties of atmosphere plasma sprayed AlCoCrFeNi high-entropy alloy coatings under post-annealing. *J. Alloys Compd.* **2021**, *872*, 159607. [CrossRef]
13. Xue, M.; Mao, X.; Lv, Y.; Chi, Y.; Yang, Y.; He, J.; Dong, Y. Comparison of Micro-nano FeCoNiCrAl and FeCoNiCrMn Coatings Prepared from Mechanical Alloyed High-entropy Alloy Powders. *J. Therm. Spray Technol.* **2021**, *30*, 1666–1678. [CrossRef]
14. Zhang, Z.; Zhang, B.; Zhu, S.; Yu, Y.; Wang, Z.; Zhang, X.; Lu, B. Microstructural characteristics and enhanced wear resistance of nanoscale Al_2O_3/13 wt%TiO_2-reinforced CoCrFeMnNi high entropy coatings. *Surf. Coat. Technol.* **2021**, *412*, 127019. [CrossRef]
15. Xiao, J.-K.; Li, T.-T.; Wu, Y.-Q.; Chen, J.; Zhang, C. Microstructure and Tribological Properties of Plasma-Sprayed CoCrFeNi-based High-Entropy Alloy Coatings Under Dry and Oil-Lubricated Sliding Conditions. *J. Therm. Spray Technol.* **2021**, *30*, 926–936. [CrossRef]

16. Zhu, S.; Zhang, Z.; Zhang, B.; Yu, Y.; Wang, Z.; Zhang, X.; Lu, B. Microstructure and Properties of Al$_2$O$_3$-13wt.%TiO$_2$-Reinforced CoCrFeMnNi High-Entropy Alloy Composite Coatings Prepared by Plasma Spraying. *J. Therm. Spray Technol.* **2021**, *30*, 772–786. [CrossRef]

17. Ma, X.; Ruggiero, P.; Bhattacharya, R.; Senkov, O.N.; Rai, A.K. Evaluation of New High Entropy Alloy as Thermal Sprayed Bondcoat in Thermal Barrier Coatings. *J. Therm. Spray Technol.* **2022**, *31*, 1011–1020. [CrossRef]

18. Sun, Z.; Zhang, M.; Wang, G.; Yang, X.; Wang, S. Wear and Corrosion Resistance Analysis of FeCoNiTiAl$_x$ High-Entropy Alloy Coatings Prepared by Laser Cladding. *Coatings* **2021**, *11*, 155. [CrossRef]

19. Wen, X.; Cui, X.; Jin, G.; Liu, Y.; Zhang, Y.; Fang, Y. In-situ synthesis of nano-lamellar Ni1.5CrCoFe0.5Mo0.1Nbx eutectic high-entropy alloy coatings by laser cladding: Alloy design and microstructure evolution. *Surf. Coat. Technol.* **2021**, *405*, 126728. [CrossRef]

20. Qiu, X. Microstructure and corrosion properties of Al$_2$CrFeCo CuNiTi high entropy alloys prepared by additive manufacturing. *J. Alloys Compd.* **2021**, *887*, 161422. [CrossRef]

21. Hussien, M.; Walton, K.; Vishnyakov, V. Synthesis and Corrosion Resistance of FeMnNiAlC$_{10}$ Multi-Principal Element Compound. *Materials* **2021**, *14*, 6356. [CrossRef]

22. Rao, S.G.; Shu, R.; Boyd, R.; le Febvrier, A.; Eklund, P. The effects of copper addition on phase composition in (CrFeCo)$_{1-y}$N$_y$ multicomponent thin films. *Appl. Surf. Sci.* **2022**, *572*, 151315. [CrossRef]

23. Cai, Z.; Wang, Z.; Yang, W.; Zhang, P.; Lu, Y.; Pu, J. Microstructure and corrosion behavior of AlCrTiV-X (X = Cu, Mo, CuMo) high-entropy alloy films in 3.5 wt.% NaCl solution. *Surf. Interfaces* **2021**, *27*, 101558. [CrossRef]

24. Chang, Y.-Y.; Chung, C.-H. Tribological and Mechanical Properties of Multicomponent CrVTiNbZr(N) Coatings. *Coatings* **2021**, *11*, 41. [CrossRef]

25. Pogrebnjak, A.; Bagdasaryan, A.; Horodeck, P.; Tarelnyk, V.; Buranich, V.; Amekura, H.; Okubo, N.; Ishikawa, N.; Beresnev, V. Positron annihilation studies of defect structure of (TiZrHfNbV)N nitride coatings under Xe14+ 200 MeV ion irradiation. *Mater. Lett.* **2021**, *303*, 130548. [CrossRef]

26. Ustinov, A.; Demchenkov, S.; Melnychenko, T.; Skorodzievskii, V.; Polishchuk, S. Effect of structure of high entropy CrFeCoNiCu alloys produced by EB PVD on their strength and dissipative properties. *J. Alloys Compd.* **2021**, *887*, 161408. [CrossRef]

27. Chen, J.; Zhou, X.; Wang, W.; Liu, B.; Lv, Y.; Yang, W.; Xu, D.; Liu, Y. A review on fundamental of high entropy alloys with promising high–temperature properties. *J. Alloys Compd.* **2018**, *760*, 15–30. [CrossRef]

28. Mazilkin, A.; Straumal, B.; Kilmametov, A.; Straumal, P.; Baretzky, B. Phase Transformations Induced by Severe Plastic Deformation. *Mater. Trans.* **2019**, *60*, 1489–1499. [CrossRef]

29. Gubicza, J.; Heczel, A.; Kawasaki, M.; Han, J.-K.; Zhao, Y.; Xue, Y.; Huang, S.; Lábár, J.L. Evolution of microstructure and hardness in Hf$_{25}$Nb$_{25}$Ti$_{25}$Zr$_{25}$ high-entropy alloy during high-pressure torsion. *J. Alloys Compd.* **2019**, *788*, 318–328. [CrossRef]

30. Čížek, J.; Haušild, P.; Cieslar, M.; Melikhova, O.; Vlasák, T.; Janeček, M.; Král, R.; Harcuba, P.; Lukáč, F.; Zýka, J.; et al. Strength enhancement of high entropy alloy HfNbTaTiZr by severe plastic deformation. *J. Alloys Compd.* **2018**, *768*, 924–937. [CrossRef]

31. Lukáč, F.; Dudr, M.; Čížek, J.; Harcuba, P.; Vlasák, T.; Janeček, M.; Kuriplach, J.; Moon, J.; Kim, H.S.; Zýka, J.; et al. Defects in High Entropy Alloy HfNbTaTiZr Prepared by High Pressure Torsion. *Acta Phys. Pol. A* **2018**, *134*, 891–894. [CrossRef]

32. Chandan, A.; Hung, P.; Kishore, K.; Kawasaki, M.; Chakraborty, J.; Gubicza, J. On prominent TRIP effect and non-basal slip in a TWIP high entropy alloy during high-pressure torsion processing. *Mater. Charact.* **2021**, *178*, 111284. [CrossRef]

33. Kilmametov, A.; Kulagin, R.; Mazilkin, A.; Seils, S.; Boll, T.; Heilmaier, M.; Hahn, H. High-pressure torsion driven mechanical alloying of CoCrFeMnNi high entropy alloy. *Scr. Mater.* **2019**, *158*, 29–33. [CrossRef]

34. Shahmir, H.; Nili-Ahmadabadi, M.; Shafiee, A.; Andrzejczuk, M.; Lewandowska, M.; Langdon, T.G. Effect of Ti on phase stability and strengthening mechanisms of a nanocrystalline CoCrFeMnNi high-entropy alloy. *Mater. Sci. Eng. A* **2018**, *725*, 196–206. [CrossRef]

35. Shahmir, H.; Nili-Ahmadabadi, M.; Shafiee, A.; Langdon, T.G. Effect of a minor titanium addition on the superplastic properties of a CoCrFeNiMn high-entropy alloy processed by high-pressure torsion. *Mater. Sci. Eng. A* **2018**, *718*, 468–476. [CrossRef]

36. Protasova, S.G.; Straumal, B.; Mazilkin, A.A.; Stakhanova, S.V.; Straumal, P.B.; Baretzky, B. Increase of Fe solubility in ZnO induced by the grain boundary adsorption. *J. Mater. Sci.* **2014**, *49*, 4490–4498. [CrossRef]

37. Straumal, B.B.; Mazilkin, A.A.; Protasova, S.G.; Stakhanova, S.V.; Straumal, P.B.; Bulatov, M.F.; Schütz, G.; Tietze, T.; Goering, E.; Baretzky, B. Grain boundaries as a source of ferromagnetism and increased solubility of Ni in nanograined ZnO. *Rev. Adv. Mater. Sci.* **2015**, *41*, 61–71.

38. Mazilkin, A.; Straumal, B.; Kilmametov, A.; Boll, T.; Baretzky, B.; Kogtenkova, O.; Korneva, A.; Zięba, P. Competition for impurity atoms between defects and solid solution during high pressure torsion. *Scr. Mater.* **2019**, *173*, 46–50. [CrossRef]

39. Ivanisenko, Y.; Sauvage, X.; Mazilkin, A.; Kilmametov, A.; Beach, J.A.; Straumal, B.B. Bulk Nanocrystalline Ferrite Stabilized through Grain Boundary Carbon Segregation. *Adv. Eng. Mater.* **2018**, *20*, 1800443. [CrossRef]

40. Nagase, T.; Iijima, Y.; Matsugaki, A.; Ameyama, K.; Nakano, T. Design and fabrication of Ti-Zr-Hf-Cr-Mo and Ti-Zr-Hf-Co-Cr-Mo high-entropy alloys as metallic biomaterials. *Mater. Sci. Eng. C* **2020**, *107*, 110322. [CrossRef]

41. Todai, M.; Nagase, T.; Hori, T.; Matsugaki, A.; Sekita, A.; Nakano, T. Novel TiNbTaZrMo high-entropy alloys for metallic biomaterials. *Scr. Mater.* **2017**, *129*, 65–68. [CrossRef]

42. Nagase, T.; Mizuuchi, K.; Nakano, T. Solidification Microstructures of the Ingots Obtained by Arc Melting and Cold Crucible Levitation Melting in TiNbTaZr Medium-Entropy Alloy and TiNbTaZrX (X = V, Mo, W) High-Entropy Alloys. *Entropy* **2019**, *21*, 483. [CrossRef]

43. Nagase, T.; Todai, M.; Hori, T.; Nakano, T. Microstructure of equiatomic and non-equiatomic Ti-Nb-Ta-Zr-Mo high-entropy alloys for metallic biomaterials. *J. Alloys Compd.* **2018**, *753*, 412–421. [CrossRef]

44. Hori, T.; Nagase, T.; Todai, M.; Matsugaki, A.; Nakano, T. Development of non-equiatomic Ti-Nb-Ta-Zr-Mo high-entropy alloys for metallic biomaterials. *Scr. Mater.* **2019**, *172*, 83–87. [CrossRef]

45. Smekhova, A.; Kuzmin, A.; Siemensmeyer, K.; Luo, C.; Chen, K.; Radu, F.; Weschke, E.; Reinholz, U.; Buzanich, A.G.; Yusenko, K.V. Al-driven peculiarities of local coordination and magnetic properties in single-phase Alx-CrFeCoNi high-entropy alloys. *Nano Res.* **2022**, *15*, 4845–4858. [CrossRef]

46. Welter, E.; Chernikov, R.; Herrmann, M.; Nemausat, R. A beamline for bulk sample X-ray absorption spectroscopy at the high brilliance storage ring PETRA III. *AIP Conf. Proc.* **2019**, *2054*, 040002. [CrossRef]

47. Kalinko, A. XAESA v0.06. 2022. Available online: https://github.com/aklnk/xaesa (accessed on 12 December 2022).

48. Ankudinov, A.L.; Ravel, B.; Rehr, J.J.; Conradson, S.D. Real-space multiple-scattering calculation and interpretation of X-ray-absorption near-edge structure. *Phys. Rev. B* **1998**, *58*, 7565–7576. [CrossRef]

49. Rehr, J.J.; Albers, R.C. Theoretical approaches to X-ray absorption fine structure. *Rev. Mod. Phys.* **2000**, *72*, 621–654. [CrossRef]

50. Kuzmin, A.; Chaboy, J. EXAFS and XANES analysis of oxides at the nanoscale. *IUCrJ* **2014**, *1*, 571–589. [CrossRef]

51. Kilmametov, A.; Ivanisenko, Y.; Straumal, B.; Mazilkin, A.; Gornakova, A.; Kriegel, M.; Fabrichnaya, O.; Rafaja, D.; Hahn, H. Transformations of α' martensite in Ti–Fe alloys under high pressure torsion. *Scr. Mater.* **2017**, *136*, 46–49. [CrossRef]

52. Kilmametov, A.; Ivanisenko, Y.; Mazilkin, A.; Straumal, B.; Gornakova, A.; Fabrichnaya, O.; Kriegel, M.; Rafaja, D.; Hahn, H. The $\alpha \rightarrow \omega$ and $\beta \rightarrow \omega$ phase transformations in Ti–Fe alloys under high-pressure torsion. *Acta Mater.* **2018**, *144*, 337–351. [CrossRef]

53. Kilmametov, A.R.; Ivanisenko, Y.; Straumal, B.B.; Gornakova, A.S.; Mazilkin, A.A.; Hahn, H. The $\alpha \rightarrow \omega$ Transformation in Titanium-Cobalt Alloys under High-Pressure Torsion. *Metals* **2018**, *8*, 1. [CrossRef]

54. Straumal, B.B.; Korneva, A.; Kilmametov, A.R.; Lityńska-Dobrzyńska, L.; Gornakova, A.S.; Chulist, R.; Karpov, M.I.; Zięba, P. Structural and Mechanical Properties of Ti–Co Alloys Treated by High Pressure Torsion. *Materials* **2019**, *12*, 426. [CrossRef]

55. Korneva, A.; Straumal, B.; Chulist, R.; Kilmametov, A.; Bała, P.; Cios, G.; Schell, N.; Zięba, P. Grain refinement of intermetallic compounds in the Cu–Sn system under high pressure torsion. *Mater. Lett.* **2016**, *179*, 12–15. [CrossRef]

56. Korneva, A.; Straumal, B.; Kilmametov, A.; Lityńska-Dobrzyńska, L.; Cios, G.; Bała, P.; Zięba, P. Effect of high pressure torsion on microstructure of Cu–Sn alloys with different content of Hume Rothery phase. *Mater. Charact.* **2016**, *118*, 411–416. [CrossRef]

57. Straumal, B.; Kilmametov, A.; Baretzky, B.; Kogtenkova, O.; Straumal, P.B.; Lityńska-Dobrzyńska, L.; Chulist, R.; Korneva, A.; Zięba, P. High pressure torsion of Cu–Ag and Cu–Sn alloys: Limits for solubility and dissolution. *Acta Mater.* **2020**, *195*, 184–198. [CrossRef]

58. Straumal, B.B.; Kilmametov, A.R.; Korneva, A.; Mazilkin, A.A.; Straumal, P.B.; Zięba, P.; Baretzky, B. Phase transitions in Cu-based alloys under high pressure torsion. *J. Alloys Compd.* **2017**, *707*, 20–26. [CrossRef]

59. Murdock, J.; Lundy, T.; Stansbury, E. Diffusion of Ti[44] and V[48] in titanium. *Acta Met.* **1964**, *12*, 1033–1039. [CrossRef]

60. Köhler, U.; Herzig, C. On the Anomalous Self-Diffusion in B.C.C. Titanium. *Phys. Status Solidi B* **1987**, *144*, 243–251. [CrossRef]

61. Hood, G.; Schultz, R. Tracer diffusion in α-Zr. *Acta Met.* **1974**, *22*, 459–464. [CrossRef]

62. Horváth, J.; Dyment, F.; Mehrer, H. Anomalous self-diffusion in a single crystal of α-zirconium. *J. Nucl. Mater.* **1984**, *126*, 206–214. [CrossRef]

63. Kidson, G.; McGurn, J. Self-diffusion in body-centered cubic zirconium. *Can. J. Phys.* **1961**, *39*, 1146–1157. [CrossRef]

64. Federer, J.I.; Lundy, I.S. Diffusion of Zr and Cb in beta zirconium. *Trans. Metall. Soc. AIME* **1963**, *227*, 592–598.

65. Herzig, C.; Eckseler, H. On the Anomalous Self-Diffusion in ß-Zirconium: Temperature Dependence of the Isotope Effect. *Int. J. Mater. Res.* **1979**, *70*, 215–223. [CrossRef]

66. Pruthi, D.D.; Agarwala, R.P. Solute and solvent diffusion in Zr-V alloys. *Philos. Mag. A* **1982**, *46*, 841–848. [CrossRef]

67. Davis, B.; McMullen, W. Bulk self-diffusion of Hf181 in monocrystalline alpha hafnium-2.1% zirconium. *Acta Met.* **1972**, *20*, 593–599. [CrossRef]

68. Winslow, E.R.; Lundy, I.S. Self-diffusion in hafnium. *Trans. Metall. Soc. AIME* **1965**, *233*, 1790–1796.

69. Herzig, C.; Manke, L.; Bussman, W. Bulk self-diffusion in hafnium. In Proceedings of the Yamada Vth Conference on Point Defects and Defect Interactions in Metals, Kyoto, Japan, 16–20 November 1981; Takamura, J.I., Doyama, M., Kiritani, M., Eds.; University of Tokyo Press: Tokyo, Japan, 1982; pp. 578–584.

70. Bronfin, M.B.; Bokshtein, S.Z.; Zhukhovitsky, A.A. Determination of diffusion coefficient using the shift of activity curve. *Zavod. Lab.* **1960**, *26*, 828–830.

71. Maier, K.; Mehrer, H.; Rein, G. Self-Diffusion in Molybdenum. *Int. J. Mater. Res.* **1979**, *70*, 271–276. [CrossRef]

72. Mundy, J.N.; Tse, C.W.; McFall, W.D. Isotope effect in chromium self-diffusion. *Phys. Rev. B* **1976**, *13*, 2349–2357. [CrossRef]

73. Mundy, J.N.; Hoff, H.A.; Pelleg, J.; Rothman, S.J.; Nowicki, L.J.; Schmidt, F.A. Self-diffusion in chromium. *Phys. Rev. B* **1981**, *24*, 658–665. [CrossRef]

74. Straumal, B.; Valiev, R.; Kogtenkova, O.; Zieba, P.; Czeppe, T.; Bielanska, E.; Faryna, M. Thermal evolution and grain boundary phase transformations in severely deformed nanograined Al–Zn alloys. *Acta Mater.* **2008**, *56*, 6123–6131. [CrossRef]

75. Straumal, B.; Klinger, L.; Shvindlerman, L. The influence of pressure on indium diffusion along single tin-germanium interphase boundaries. *Scr. Met.* **1983**, *17*, 275–279. [CrossRef]
76. Molodov, D.; Straumal, B.; Shvindlerman, L. The effect of pressure on migration of 001 tilt grain boundaries in tin bicrystals. *Scr. Met.* **1984**, *18*, 207–211. [CrossRef]
77. Molodov, D.; Swiderski, J.; Gottstein, G.; Lojkowski, W.; Shvindlerman, L. Effect of pressure on grain boundary migration in aluminium bicrystals. *Acta Met. Mater.* **1994**, *42*, 3397–3407. [CrossRef]
78. Muller, J.E.; Jepsen, O.; Andersen, O.K.; Wilkins, J.W. Systematic Structure in the K-Edge Photoabsorption Spectra of the4dTransition Metals: Theory. *Phys. Rev. Lett.* **1978**, *40*, 720–722. [CrossRef]
79. Müller, J.; Jepsen, O.; Wilkins, J. X-ray absorption spectra: K-edges of 3d transition metals, L-edges of 3d and 4d metals, and M-edges of palladium. *Solid State Commun.* **1982**, *42*, 365–368. [CrossRef]
80. Keski-Rahkonen, O.; Krause, M.O. Total and partial atomic-level widths. *At. Data Nucl. Data Tables* **1974**, *14*, 139–146. [CrossRef]
81. Qi, B.; Perez, I.; Ansari, P.H.; Lu, F.; Croft, M. L2 and L3 measurements of transition-metal 5d orbital occupancy, spin-orbit effects, and chemical bonding. *Phys. Rev. B* **1987**, *36*, 2972–2975. [CrossRef]